Chinese Chemical Letters 33 (2022) 1417–1421

Contents lists available at ScienceDirect

Chinese Chemical Letters

journal homepage: www.elsevier.com/locate/cclet

Single molecule magnetic behavior and photo-enhanced proton conductivity in a series of photochromic complexes

Qian Zhang, Jixiang Hu*, Qi Li, Dongxue Feng, Zhenni Gao, Guoming Wang*

College of Chemistry and Chemical Engineering, Qingdao University, Qingdao 266071, China

ARTICLE INFO

Article history:
Received 7 July 2021
Revised 17 July 2021
Accepted 7 August 2021
Available online 12 August 2021

Keywords:
Multifunctional
Electron transfer
Photochromism
Single molecule magnetic behavior
Proton conductivity

ABSTRACT

Molecules with multifunctional properties are of immense interest in hybrid materials, while challenges still existed because of the limited compatibility of multiple functionalities in a single system. In this work, a series of metal-organic complexes were synthesized and characterized under the assembly of electron donor phosphonate, electron acceptor polypyridine ligand and spin carrier rare earth ions. All the compounds exhibited remarkable and reversible responses with photochromism and photomodulated fluorescence, originated from photogenerated radicals *via* electron transfer from phosphonates to polypyridine ligands. For the Dy analog, slow magnetic relaxation was observed at cryogenic temperature, indicating the single-molecule magnetic behavior. Furthermore, photogenerated radicals could enhance the proton conductive behavior, with about 2 times larger in magnitude after light irradiation for Dy and Y compounds. The introduction of photoluminescence, magnetism and proton conduction into metallic phosphonates can provide potential applications for photochromic materials.

The field of chemistry and materials science has witnessed a boom of multifunctional materials in recent years [1–6]. As promising candidates for smart materials, the multifunctional metal-organic complexes (MOCs) could be potentially utilized in across areas of optical switching, sensing, energy storage, *etc.* Meanwhile, the switch that can be realized in the MOCs *via* external stimuli, such as light, temperature, humidity, and electrical/magnetic fields, provides unique opportunities for elucidating structure-function relationships and future applications [7–13]. Light irradiation has been demonstrated as a powerful method for the dynamic control of these MOCs. In this aspect, electron transfer photochromic MOCs create more opportunities and provide a new strategy for researchers to design photochromic materials with a variety of potential functions. The combined bifunctional properties including semiconductors, magnetism, phosphorescence, proton conductivities and nonlinear optical properties have been realized in these electron transfer photochromic MOCs [14–21]. However, the multiple functionalities, especially quadruple response of light actuated chromism, photoluminescence, single molecule magnets and proton conductivity in the same crystalline matter, has still a challenge for now.

Metallic phosphonates, as an important class of MOCs, have manifold coordination modes and strong coordination ability, showing a variety of structure types and interesting properties [22–24]. On the one hand, the electron-rich phosphonate components could be efficiently utilized as electron donors when assembly with the electron-deficient polypyridine derivatives, making them as a hot branch in the field of electron transfer photochromic MOCs. On the other hand, electron-rich O atoms in metal-phosphonates can further provide the main proton sources and are likely to be the crucial factor for the high proton conductivity. Since the O atoms on the organic phosphonic acid ligand can coordinate with metal ions to form a multi-structure framework, they can also act as donors or/and acceptors of hydrogen bonds to form hydrogen bonding networks with the guest molecule or other ligands, providing abundant transport paths for proton conduction in these MOCs. Combined with its good thermal/water stability and clear structure for exploring the proton conductive mechanism, these metal-phosphonates attract much attention for pursuing proton conductive materials with high performance [25–27]. Furthermore, lanthanide ions with their unique 4f electrons render them as the ideal candidates for assembling multifunctional MOCs [28–30]. Due to their larger magnetic anisotropy and intrinsic strong spin-orbit coupling interactions than transition metal ions, these lanthanide ions are widely exploited for constructing single-molecule magnets (SMMs) with a high relaxation barrier [31–35].

* Corresponding authors.
E-mail addresses: hujixiang@qdu.edu.cn (J. Hu), gmwang_pub@163.com (G. Wang).

https://doi.org/10.1016/j.cclet.2021.08.029
1001-8417/

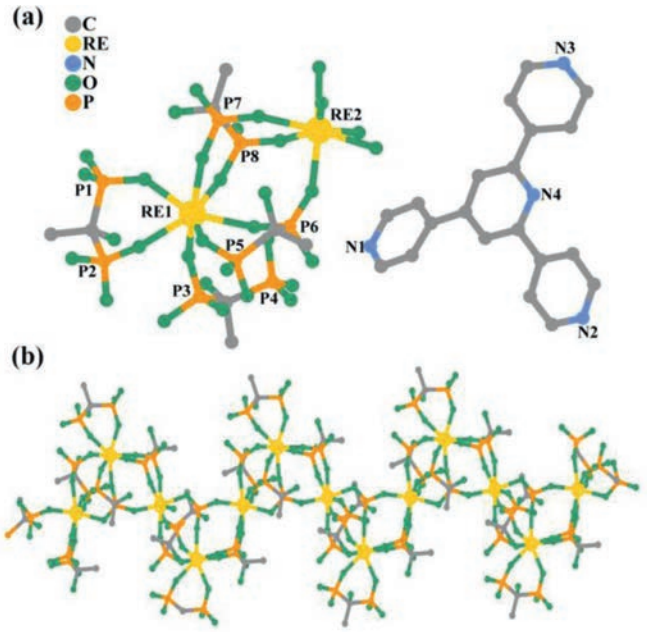

Fig. 1. (a) Asymmetric unit of the isostructural compounds. (b) The RE-diphosphonate chain. Atom legend: P, light orange; N, blue; O, sea green; C, gray-40%; RE, gold. H atoms and water molecules are omitted for clarity.

Based on the above considerations, we have synthesized and characterized a series of one-dimensional MOCs [RE_2(H-HEDP)(H_2-HEDP)$_3$]·H_3-TPP·9H_2O (RE = Dy for **1**; Tb for **2**; Y for **3** and Er for **4**; HEDP = hydroxyethylidene diphosphonate, TPP = 2,4,6-tris(4-pyridyl)pyridine) under the assembly of electron rich organic phosphonic acid, a new electron-deficient and photoactive polypyridine ligand and spin carrier rare earth ions. *Via* Xenon lamp irradiation, these photoactive compounds show remarkable coloration with colorless crystal changed to blue. The photochromism actuated from photogenerated radicals was an electron transfer process from diphosphonate chain, to protonated TPP components, as verified by UV-vis and electron spin resonance spectra. Photoluminescence measurements show direct and sharp decreases in luminescence intensity with the duration of light. For the Dy analog, detectable slow magnetic relaxation was observed at cryogenic temperature, indicating the single-molecule magnetic behavior. Moreover, due to the presence of the hydrophilic channel and a large number of hydrogen bonding interactions through the framework, proton conductivities for **1** and **3** were performed as examples under 100% relative humidity. After illumination, the values of proton conductivity in the temperature measurement region increased obviously, indicating photo improved proton conductive behaviors of these photochromic chain compounds.

Single-crystal X-ray diffraction (XRD) experiments uncover a series of isostructural chains, as they all crystallize in the same *C*2/*c* space group (Table S1 in Supporting information), only compound **1** is discussed here for clarity. As depicted in Fig. 1a, each asymmetric unit contains two crystallographically unique Dy^{3+} ions, four electron-rich diphosphonate units, one electron-deficient TPP cation, and nine free water molecules. The crystal field for each Dy^{3+} ion indicates anisotropy with the Dy-O bonds range 2.2627(2)–2.39904(8) Å and 2.22182(8)–2.4000(2) Å for Dy1 and Dy2 (Table S2 in Supporting information), respectively, probably beneficial for the SMM behavior. Each [DyO_7] core geometry with all O atoms from four separate HEDP units adopted a capped trigonal prism (C2v) (Tables S6-S9 in Supporting information), which is calculated with the SHAPE 2.0 program [36]. The distinct HEDP components, acting as chelating and bridging ligands, respectively, further bridged two adjacent Dy^{3+} cations to form an infinite zigzag chain (Fig. 1b). The nearest intrachain and interchain Dy···Dy distances is 4.9518(7) and 12.7508(13) Å, respectively, suggesting that the intrachain interaction are dominant with a negligible interchain dipole-dipole interaction. Hydrogen bonding interactions with the distances of 2.5674(9)–3.2982(7) Å are formed among HEDP chains, protonated TPP ligands and isolated water molecules, providing an abundant electron and proton transfer path for photochromism and proton conduction. These chains are further connected by hydrogen bonds and form a three-dimensional network (Fig. S1 in Supporting information). The bonds and angles of compounds **2**–**4** are similar with **1** and listed in Tables S3–S5 (Supporting information).

Powder X-ray diffraction experiments show that the measured peaks are in good agreement with the simulated PXRD, indicating the high purities of crystal phases in all the compounds (Fig. S2 in Supporting information). Thermogravimetric analyses (TGA) in nitrogen flow revealed that **1** undergoes a two-step weight loss upon heating (Fig. S3 in Supporting information). Before 152 °C, the desorption of nine free water molecules results in a first weightlessness of 9.98 wt%. After experiencing a platform, the framework begins to collapse from 220 °C with the decomposition of HEDP and TPP organic ligands.

As a new photoactive electron acceptor unit, the photochromic behavior of the TPP itself is firstly explored at solid state. After Xenon lamp light illumination for 30 min, the light grey TPP powders turn to faint yellow (Fig. S4 in Supporting information), showing the characteristics of photoactivity. The solid-state UV-vis and photoluminescence spectra are recorded to quest the light-induced color variations. As shown in Figs. S5 and S6 (Supporting information), a broad peak centered at 573 nm appears and increases in UV-vis spectra while a direct decrease occurs in emission spectra as the irradiation continued, suggesting the generation of TPP$^{\bullet}$ radicals. Similar with the reported polypyridine-based photochromic complexes, the compounds constructed by this new photochromic ligand also show photoactive behavior with clear color changes. As shown in Fig. S7 (Supporting information), all the crystal compounds show eye-detectable photochromic transformation from colorless to blue upon Xenon lamp irradiation. The irradiated blue samples can then return to the initial colorless states *via* being stayed in the dark at room temperature for several days or by heating at 120 °C in air for 12 h. The discolored samples also displayed color changes after irradiation again, discovering the high reversibility of this photochromic behavior. The PXRD and IR spectra for all the compounds after irradiation are measured and without significant variations (Figs. S2 and S8 in Supporting information), indicating that these photochromic transitions are originated from the photogenerated radicals and irrelevant with structural transformation or photolysis, as observed in many other electron transfer photochromic materials [37–39].

Their photochromic behaviors were firstly characterized by solid state UV-vis spectra. As depicted in Fig. 2, the irradiated samples show nearly the same characteristic bands around 572 nm for **1**–**4** in the UV-vis spectra, and their intensities gradually increase as the irradiation time increased. For **4**, the additional absorption peaks are assigned to the $^4I_{15/2}\rightarrow{}^4G_{11/2}$ (378 nm), $^4I_{15/2}\rightarrow{}^4F_{7/2}$ (489 nm), $^4I_{15/2}\rightarrow{}^2H_{11/2}$ (521 nm) and $^4I_{9/2}\rightarrow{}^2K_{15/2}$ (652 nm) transitions of Er^{3+}. After decoloration, these characteristic peaks disappear again, further suggesting the reversible photochromism. In view of detectable broad bands after illumination in the region of 480–610 nm for TPP ligand (Fig. S5), these enhanced absorptions for all the compounds presumably arose from the production of the H_3-TPP$^{\bullet}$ radicals. To test this hypothesis, the electron spin resonance (ESR) analyses were introduced to quest photogenerated radicals before and after irradiation under the same conditions. As shown in Fig. S9 (Supporting information), the ESR spectrum

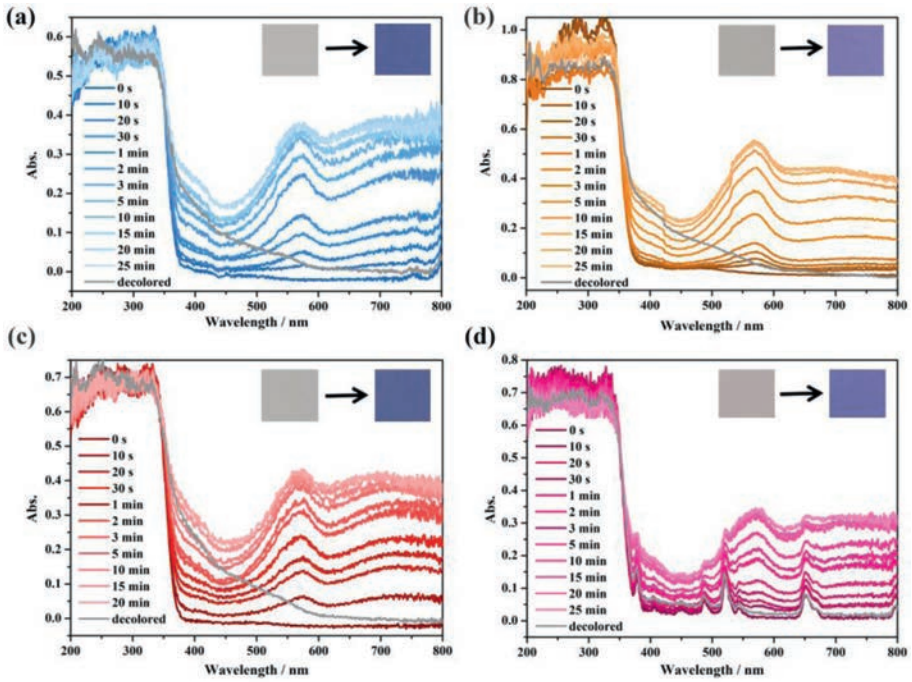

Fig. 2. Time-dependent UV-vis spectra of the original, irradiated and decolored samples (a) **1**, (b) **2**, (c) **3** and (d) **4**. Insert: the photos of the coloration process upon irradiation.

between 500 and 6500 G reveal the characteristic signal of the rare earth metal ions in the original samples, while a sharp signal around 3500 G is observed after irradiation, with the *g* value of 1.9995, 2.0037, 2.0037 and 2.0032 for **1**–**4**, respectively. These results demonstrate that compounds **1**–**4** exhibit radical-actuated photochromic properties.

Since the photogenerated radicals can influence the fluorescence properties of the complexes, solid state photoluminescence spectra of all the complexes were performed under ambient conditions. Upon excitation at 272 nm for **1**, the emission spectrum exhibits strong fluorescence emission at 373 nm, which should be assigned to the $\pi \rightarrow \pi^*$ intraligand fluorescence emission of TPP, as confirmed in this ligand's spectra (Fig. S6) and other compounds containing 2,4,6-tris(4-pyridyl)pyridine [40]. The strong emission peak also appears at 482 nm, corresponding to $^4F_{9/2} \rightarrow {}^6H_{15/2}$ transition of the Dy^{3+} centers in **1**. Upon continuous irradiation by Xenon lamp, the emission intensities of compound **1** decrease gradually accompanied with the color of powder samples gradually changed to blue (Fig. S10 in Supporting information). After being irradiated for 60 min, the intensity of the main peak sharply decreases to 30 % of the initial value, indicating that photogenerated radicals result in an overlap of emission band and absorption band, and finally quench the photoluminescent behavior. The rest compounds also exhibited the similar photoluminescence quenching during coloration.

The dc magnetic susceptibility measurements for complex **1** are explored between 2 K and 300 K in the presence of 1 kOe external magnetic field (Fig. S11 in Supporting information). The experimental χT value of compound **1** is 28.04 cm^3 K/mol at 300 K, which is slightly lower than the expected theoretical value of 28.34 cm^3 K/mol for two non-interacting Dy^{3+} ($S = 5/2$, $L = 5$, $g = 4/3$). Originated from thermal depopulation of the excited stark sublevels of the anisotropic Dy^{3+}, the curve on cooling mode directly declines to a minimum value 20.53 cm^3 K/mol at 2 K. The field dependence of magnetization *M vs. H* for complex **1** is measured at 2 K, with the *M* values gradually reach to 10.94 Nβ at 50 kOe (Fig. S12 in Supporting information). For further quest the magnetization relaxation dynamics of **1**, ac magnetic susceptibilities are measured under a zero dc and 3.5 Oe ac field. As shown in Fig. S13 (Supporting information), in the frequency-dependent ac susceptibility data, both the in-phase (χ') and out-of-phase (χ'') components exhibit frequency dependence, showing the slow magnetic relaxation and might be an indication of SMM. However, similar to other reported Dy-based complexes [41–43], no peaks for both χ' and χ'' components are observed down to 2 K, which should be originated from fast quantum tunnelling of magnetization (QTM). Assuming only one characteristic relaxation process of the Debye type occurred in **1**, the Debye model is thus employed to estimate the energy barrier Ea/k_B and τ_0 based on the relationship $\ln(\chi''/\chi') = \ln(\omega\tau_0) + Ea/k_BT$ (Fig. S14 in Supporting information). Best linear fit to the experimental data yields $Ea/k_B = 15.4$ K and $\tau_0 = 8.9 \times 10^{-6}$ s, consistent with a superparamagnetic-like character of the relaxation dynamics and confirming the SMM behavior [44–46]. Since the tunneling mechanism might be suppressed by an additional field [47], a 2 kOe dc field is introduced to further perform the ac susceptibility measurements. As shown in Fig. 3, χ' signals are more visible and show frequency dependent peaks, while the peak of χ'' components is still not observed, indicating that the strong quantum tunneling effect was minimized but not effectively suppressed. Furthermore, the magnetization relaxation dynamics after light irradiation are also explored since photogen-

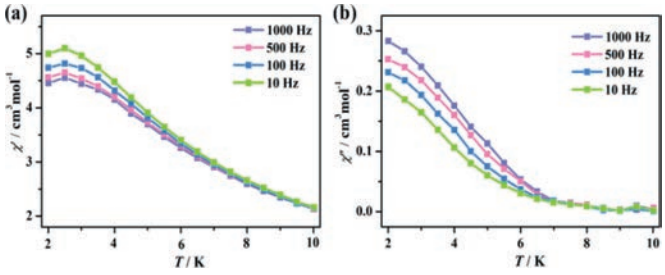

Fig. 3. Plots of χ' (a) and χ'' (b) *versus T* for compound **1** in a 2000 Oe dc field.

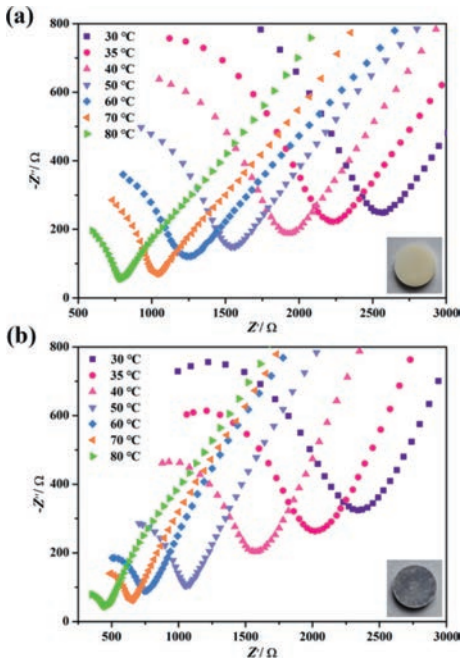

Fig. 4. Time Nyquist plots of impedance spectra of **1** (a) and **1a** (b) at 100% RH and different temperatures ranging from 303 K to 353 K.

erated radicals as another spin carriers introduced to this chain system may magnetically couple with Dy^{3+} centers. However, no obvious variations detected in the dc and ac susceptibility measurements (Figs. S11 and S15 in Supporting information). The neglectable changes of susceptibility data in this photomagnetic measurements may be due to the weakly magnetic couplings between Dy^{3+} and photogenerated radicals, originated from shielding effect of 4f orbitals in Dy^{3+} centers and relatively long distances between Dy^{3+} ions and $TPP^{\bullet}$ radicals. The magnetic properties for other compounds were also measured while no SMM behavior was observed.

Due to the abundant water-filled channels, good thermal/water stability, these series of compounds could be utilized as potential proton conductors. Obviously, large numbers of hydrogen bonding interactions formed in this chain structure, with the average O···O and O···N distances of 2.832 Å among lattice water molecules, HEDP components and TPP cations (Tables S10–S13 in Supporting information). These remarkable hydrogen bond networks could be in favor of the proton transfer, further resulting in enhanced proton conductivity. The AC impedance of the pressed sample of compound **1** is measured at 100% RH and different temperatures. The proton conductivities are calculated from the fitting of the Nyquist plots. As shown in Fig. 4 and Table S14 (Supporting information), all Nyquist diagrams show incomplete semicircles and sloping tails at high and low frequencies, respectively exhibiting the characteristic bulk and grain boundary resistances of proton conductors. The initial proton conductivity is determined as 9.33×10^{-5} S/cm at 30°C, then the conductivities increased with the resistance values decreased upon heating, showing a typical proton conducting behavior. The optimized proton conductivities for **1** reach to be 3.06×10^{-4} S/cm at 80 °C, with the magnitude about 3 times than the initial value. The activation energy of compound **1** calculated by Arrhenius equation is 0.23 eV. This value implies that the proton conduction process mainly follows the typical Grotthus mechanism with proton hops in the hydrogen bond channels (< 0.4 eV) [48,49].

To further explore the effect of photogenerated free radicals on the proton conductivity, the irradiated blue **1a** sample are used for AC impedance measurement under the same conditions. As shown in Table S14, the conductivities of **1a** in the measured temperature regions show an average increase about 100% than **1**. This indicated that photoinduced stable free radicals could promote proton conduction, resulting in an increase in overall electrical conductivity. The fitted activation energy of 0.40 eV (Fig. S16 in Supporting information) suggested the dominated Grotthus mechanisms in **1a**, and vehicle mechanisms may begin to participate in the proton transfer process. Upon coloration, H^+ in H_3-TPP components may be easily dissociated upon forming the stable $TPP^{\bullet}$ radicals, the increased protons offer more hydrogen bonding networks and further contribute to the improved proton conductivities. After measured these conductivities before and after light irradiation, the samples still remain the frame structures, as confirmed by the PXRD patterns of the pressed samples (Fig. S17 in Supporting information). Due to the isostructural compounds, the impedance of complex **3** is also performed as an example and exhibit a similar behavior with **1** (Figs. S18 and S19 in Supporting information). At 100% RH and 80°C, the proton conductivity reached 2.90×10^{-4} S/cm and 6.34×10^{-4} S/cm for **3** and **3a** (Table S15 in Supporting information), respectively, showing a photogenerated radicals actuated conductivity enhancement behavior.

In conclusion, *via* association of phosphonate donor, TPP acceptor and rare earth spin carriers under hydrothermal conditions, a quadruple functionality with photochromism, photoluminescence, SMM behavior and photo-enhanced proton conductivity was achieved in a series of rare earth phosphonates. The coloration behavior is induced by photogenerated radicals originated from electron transfer process from diphosphonate chain to protonated TPP components. Light irradiation also induces large decreases in luminescence intensity, showing the photoluminescence quenching effect for all the compounds. For the Dy analog, detectable slow magnetic relaxation is observed at cryogenic temperatures, indicating the single-molecule magnetic behavior. Moreover, due to the presence of the hydrophilic channel and a large number of hydrogen bonding interactions through the framework, proton conductivities for **1** and **3** are performed under 100% relative humidity. After light irradiation, the proton conductivity values show obvious increases at the measured temperature region with an average 100% increase in magnitude, exhibiting light enhanced proton conductivity in these series of photochromic chain compounds. This work innovatively reveals a kind of MOC material which integrates photochromic, photoluminescence, SMM and proton conduction, providing an idea for the development of intelligent molecular materials with reconfigurable properties in molecular devices and sensors.

Declaration of competing interest

The authors declare that they have no known competing financial interests or personal relationships that could have appeared to influence the work reported in this paper.

Acknowledgments

This work was supported by the National Natural Science Foundation of China (Nos. 21901133 and 22071126), Key Research and Development Project of Shandong Province (No. 2019GGX102006) and the State Key Laboratory of Fine Chemicals (No. KF1905).

Supplementary materials

Supplementary material associated with this article can be found, in the online version, at doi:10.1016/j.cclet.2021.08.029.

References

[1] B. Li, H.M. Wen, Y.J. Cui, et al., Adv. Mater. 28 (2016) 8819–8860.
[2] R. Gao, D. Cao, Y. Guan, D. Yan, ACS Appl. Mater. Interfaces 7 (2015) 9904–9910.
[3] B. Lv, Z. Wu, C. Ji, et al., J. Mater. Chem. C 3 (2015) 8519–8525.
[4] H.Y. Wang, J.Y. Ge, C. Hua, et al., Angew. Chem. Int. Ed. 56 (2017) 5465–5470.
[5] Z.Z. Xue, X.D. Meng, X.Y. Li, et al., Inorg. Chem. 60 (2021) 4375–4379.
[6] B. Lu, S. Liu, D. Yan, Chin. Chem. Lett. 30 (2019) 1908–1922.
[7] X. Yang, X. Lin, Y.S. Zhao, D. Yan, Chem. Eur. J. 24 (2018) 6484–6493.
[8] B. Zhou, G. Xiao, D. Yan, Adv. Mater. 33 (2021) 2007571.
[9] W. Zhang, R.G. Xiong, Chem. Rev. 112 (2012) 1163–1195.
[10] Y.S. Meng, O. Sato, T. Liu, Angew. Chem. Int. Ed. 57 (2018) 12216–12226.
[11] X.D. Huang, G.H. Wen, S.S. Bao, J.G. Jia, L.M. Zheng, Chem. Sci. 12 (2021) 929–937.
[12] Y. Xiao, B. Li, Z.X. You, et al., J. Mater. Chem. C 9 (2021) 3193–3203.
[13] J.H. Qin, Y.D. Huang, Y. Zhao, et al., Inorg. Chem. 58 (2019) 15013–15016.
[14] G.E. Wang, G. Xu, N.N. Zhang, et al., Angew. Chem. Int. Ed. 58 (2019) 2692–2695.
[15] Q. Li, Q. Zhang, W.J. Wei, et al., Chem. Commun. 57 (2021) 4295–4298.
[16] H.Y. Li, Y.L. Wei, X.Y. Dong, S.Q. Zang, T.C.W. Mak, Chem. Mater. 27 (2015) 1327–1331.
[17] S.D. Han, A.J. Liu, Q. Wei, et al., Chem. Eur. J. 27 (2021) 7842–7846.
[18] A.J. Liu, F. Xu, S.D. Han, J. Pan, G.M. Wang, Cryst. Growth Des. 20 (2020) 7350–7355.
[19] S. Sun, Q. Wei, Y. Huang, et al., J. Mater. Chem. C 8 (2020) 7104–7112.
[20] Q. Zhang, W.J. Wei, Q. Li, et al., Sci. China Chem. 64 (2021) 1170–1176.
[21] X.S. Xing, R.J. Sa, P.X. Li, et al., Chem. Sci. 8 (2017) 7751–7757.
[22] S.S. Bao, G.K.H. Shimizu, L.M. Zheng, Coord. Chem. Rev. 378 (2019) 577–594.
[23] Y.Y. Zhu, Y.A. Zhou, X. Zhang, Z.A. Sun, C.Q. Jiao, Adv. Opt. Mater. 9 (2021) 2001889.
[24] J.X. Hu, X.F. Jiang, Y.J. Ma, et al., Sci. China Chem. 64 (2021) 432–438.
[25] L. Vilčiauskas, M.E. Tuckerman, G. Bester, S.J. Paddison, K.D. Kreuer, Nat. Chem. 4 (2012) 461–466.
[26] S. Zhang, Y. Lu, X.W. Sun, et al., Chem. Commun. 56 (2020) 391–394.
[27] D. Umeyama, S. Horike, M. Inukai, T. Itakura, S. Kitagawa, J. Am. Chem. Soc. 134 (2012) 12780–12785.
[28] J. Huo, A. Yu, Q. Ni, et al., Inorg. Chem. 59 (2020) 15514–15525.
[29] M. Chen, Q. Wen, F. Gu, et al., Chem. Eng. J. 342 (2018) 331–338.
[30] Z. Zhou, C.C. Zhang, Y. Zheng, Q. Wang, Dyes Pigment. 150 (2018) 151–157.
[31] R. Sessoli, A.K. Powell, Coord. Chem. Rev. 253 (2009) 2328–2341.
[32] D.N. Woodruff, R.E.P. Winpenny, R.A. Layfield, Chem. Rev. 113 (2013) 5110–5148.
[33] Y.S. Meng, S.D. Jiang, B.W. Wang, S. Gao, Acc. Chem. Res. 49 (2016) 2381–2389.
[34] K. Liu, X. Zhang, X. Meng, et al., Chem. Soc. Rev. 45 (2016) 2423–2439.
[35] J.L. Liu, Y.C. Chen, M.L. Tong, Chem. Soc. Rev. 47 (2018) 2431–2453.
[36] D. Casanova, J. Cirera, M. Llunell, et al., J. Am. Chem. Soc. 126 (2004) 1755–1763.
[37] S.L. Li, M. Han, Y. Zhang, et al., J. Am. Chem. Soc. 141 (2019) 12663–12672.
[38] C. Chen, J.K. Sun, Y.J. Zhang, X.D. Yang, J. Zhang, Angew. Chem. Int. Ed. 56 (2017) 14458–14462.
[39] Q. Sui, X.T. Ren, Y.X. Dai, et al., Chem. Sci. 8 (2017) 2758–2768.
[40] B.C. Wang, Q.R. Wu, H.M. Hu, et al., CrystEngComm 12 (2010) 485–492.
[41] H.S. Ke, G.F. Xu, L. Zhao, et al., Chem. Eur. J. 15 (2009) 10335–10338.
[42] M.T. Gamer, Y.H. Lan, P.W. Roesky, A.K. Powell, R. Clérac, Inorg. Chem. 47 (2008) 6581–6583.
[43] M. Zhu, Y. Li, L.J. Jia, L. Zhang, W. Zhang, RSC Adv. 7 (2017) 36895–36901.
[44] Y.N. Guo, G.F. Xu, L. Zhao, et al., J. Am. Chem. Soc. 132 (2010) 8538–8539.
[45] S. Mukherjee, J.J. Lu, G. Velmurugan, et al., Inorg. Chem. 55 (2016) 11283–11298.
[46] H.D. Li, J. Sun, M. Yang, et al., New J. Chem. 41 (2017) 10181–10188.
[47] S.D. Han, X.H. Miao, S.J. Liu, X.H. Bu, Inorg. Chem. Front. 1 (2014) 549–552.
[48] S. Chand, S.C. Pal, A. Pal, et al., Chem. Eur. J. 25 (2019) 1691–1695.
[49] L.J. Huang, L. Wang, Y. Zhao, et al., Dalton Trans. 49 (2020) 5440–5444.